

pubs.acs.org/JPCA Article

Combined Experimental and Computational Kinetics Studies for the Atmospherically Important BrHg Radical Reacting with NO and O₂

Rongrong Wu, Pedro J. Castro, Cameron Gaito, Kyle Beiter, Theodore S. Dibble,* and Chuji Wang*



Cite This: https://doi.org/10.1021/acs.jpca.2c02531



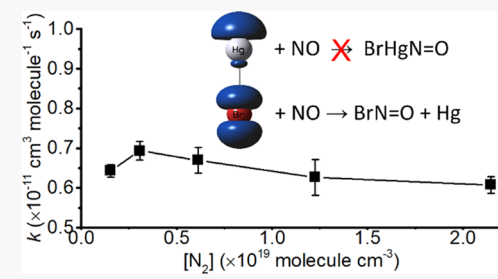
ACCESS

Metrics & More

Article Recommendations

s Supporting Information

ABSTRACT: We report on the first experimental determination of the absolute rate constant of the reaction of BrHg + NO in N₂ bath gas using a laser photolysis—laser-induced fluorescence (LP-LIF) system. The rate constant of the reaction of BrHg + NO is determined to be $7.0^{+1.3}_{-0.9} \times 10^{-12}$ cm³ molecule⁻¹ s⁻¹ over 50–700 Torr and 315–353 K. The absence of a pressure or temperature dependence suggests that this reaction leads mainly to mercury reduction (Hg + BrNO) rather than mercury oxidation (BrHgNO). Our theoretical calculations using NEVPT2 energies on density functional theory (DFT) geometries are consistent with a barrierless reaction to form Hg + BrNO. The equilibrium constants and the rate constants of the reaction BrHg + O₂ \rightleftharpoons BrHgOO are



computed theoretically because they are too low to be measured in the LP-LIF system. Molecular oxygen quenches the LIF signal of BrHg with a large rate constant of $(1.7 \pm 0.1) \times 10^{-10}$ cm³ molecule⁻¹ s⁻¹. Thus, different techniques that capture the absolute [BrHg(\tilde{X})] would be advantageous for kinetics studies of BrHg reactions in the presence of O₂. The computed equilibrium constant suggests a non-negligible upper limit of the fraction of BrHg stored as BrHgOO (up to 0.5) at low-temperature conditions, e.g., in the upper troposphere and in polar winters at ground level. Preliminary results indicate that BrHgOO behaves like HOO or organic peroxy radicals in reactions with atmospheric radicals.

I. INTRODUCTION

Mercury is a pollutant of global concern due to its long atmospheric lifetime (0.5–1 year), enabling long-range transportation via the atmosphere. Deposition from the atmosphere to ecosystems is followed by bioaccumulation and biomagnification to neurotoxic levels that harm the wellbeing of animals and humans. ^{1–4} Atmospheric mercury is primarily emitted as gaseous elemental mercury (GEM, Hg⁽⁰⁾) by anthropogenic and natural sources, as well as reemissions. ^{1,3} However, gaseous oxidized mercury (GOM), mostly as divalent mercury (Hg^(II)), is more prone than GEM to wet deposition or dry deposition in oceans, due to its higher water solubility and lower vapor pressure. ^{3,5} So mercury primarily enters ecosystems as Hg^(II).

In the atmosphere, Hg cycles among elemental Hg⁽⁰⁾, oxidized monovalent Hg⁽¹⁾, and divalent Hg^(II). Atomic bromine (Br) is considered the main oxidant, and the oxidation of Hg⁽⁰⁾ by ozone (O₃) or the hydroxyl radical (OH) is inefficient since the Hg⁽¹⁾ products of these reactions are weakly bound. Br-initiated Hg⁽⁰⁾ oxidation to Hg^(II) proceeds via a two-step process: first, Hg⁽⁰⁾ reacts with atomic Br to produce BrHg radicals, A Hg⁽¹⁾ intermediate that can photolytically or thermally decompose back to Hg⁽⁰⁾, 6,9,12 second, BrHg reacts with other radicals, such as HOO, NO₂, Br, OH, and BrO, to form inorganic oxidized Hg^(II) compounds. A Hg^(II) Field and modeling studies indicate that Br-initiated oxidation dominates in a range of environments, including the polar regions, salt lakes, tropical marine boundary

layer, and the free troposphere, where Br chemistry is active and Br is relatively abundant. The most recent theoretical and experimental kinetics studies have shown that BrHg could react with $\rm O_3$ to produce BrHgO + $\rm O_2$. Reaction with ozone would dominate the oxidation of Hg $^{(II)}$ and enable the OH radical to initiate Hg $^{(0)}$ oxidation via HOHg. 9,10,24,25

We are still unveiling the major aspects of the redox chemistry of atmospheric mercury. Recent theoretical calculations have found that the major divalent species (BrHgOOH, BrHgOH, BrHgONO, etc.) strongly absorb UV light, leading to fast photolysis (mostly photoreduction) in the gaseous phase, which dominates the reduction of oxidized mercury in the atmosphere. ^{12,24,25,27-31} Hg^(II) species can be absorbed and dissolved by aqueous particles/cloud droplets and become Hg²⁺ ions, which form complexes with various ligands, such as halides and organic groups. ³² Aqueous-phase photoreduction can also occur. ³³⁻³⁵ The presence of high [Cl⁻] may lead particles to emit HgCl₂ to the gas phase. ³⁶ GOM can also be absorbed on dry particles, where photoreduction may also

Received: April 12, 2022 Revised: May 22, 2022



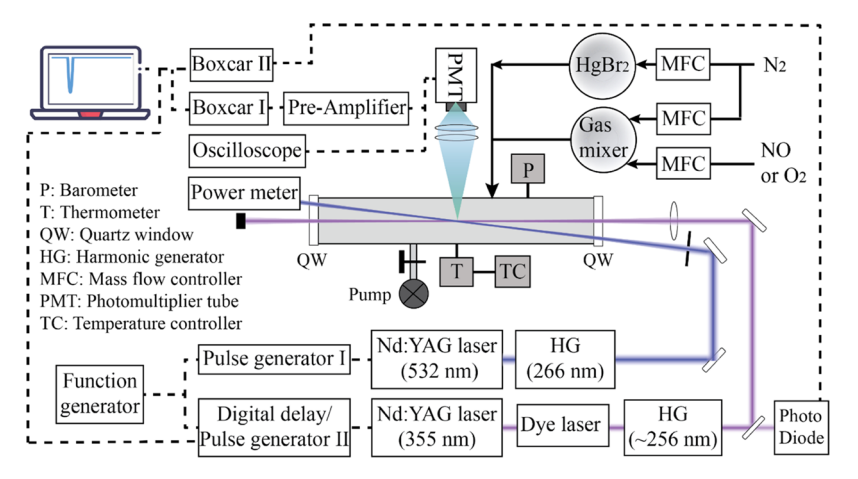


Figure 1. Schematic of the LP-LIF system.

occur. 37,338 Reduction of gas-phase Hg^(II) and Hg^(I) radicals can occur in thermal reactions, such as BrHgO reacting with CO to produce BrHg and CO₂, 39 and BrHg reacting with NO₂ to produce Hg⁽⁰⁾ and BrNO₂. 16,17 O₃ potentially reduces HgBr₂/HgCl₂ to Hg⁽⁰⁾ under irradiation, according to a new laboratory result. 40 Most of these gas-phase reduction reactions are only known from computational chemistry and have not been validated by experiments. Most of the aqueous-phase and surface-based photoreduction reactions have only been studied empirically and lack a solid mechanistic basis. These factors limit our understanding of mercury redox chemistry, which hinders efforts to predict how emission reductions impact the spatial distribution of mercury entry into ecosystems. 2,10,41–44

The kinetics of the reaction between BrHg and NO have not been studied theoretically or experimentally. A previous thermodynamics study has shown that BrHg-NO bond is weak (12 kcal mol⁻¹) so that BrHgNO would rapidly undergo thermal dissociation. ^{13,14} This means that NO is unable to effectively oxidize BrHg. We are interested in whether the reaction of BrHg and NO could lead to Hg⁽¹⁾ reduction

$$BrHg + NO \rightarrow Hg + BrNO$$
 (R1)

analogous to the reduction channel of the reaction of BrHg + NO_2 . 16,17 We report here on our combined experimental and theoretical study of the new reduction reaction R1. The rate constant of this reduction pathway is measured as a function of temperature and pressure using the laser photolysis—laser-induced fluorescence (LP-LIF) system used in the previous kinetics study for the reaction of BrHg + NO_2 and O_3 . 10,17 We also have used computational chemistry to determine the potential energy profile for this reaction and compute the rate constant versus temperature.

Similarly, the kinetics of the reaction between BrHg and O_2 have not been studied theoretically or experimentally. A previous thermodynamics study has suggested that the reaction of BrHg + O_2 is unlikely to result in much BrHgOO due to the weak BrHg–OO bond (computed at 7 kcal mol⁻¹). Furthermore, the reaction of BrHg with O_2 to produce BrOO and Hg, analogous to reaction R1, is endothermic since the enthalpies of formation at 298 K for BrHg, O_2 , BrOO, and Hg are 24.9 \pm 2.4, 0.00, 28.6 \pm 1.4, and 14.67 \pm 0.01 kcal mol⁻¹, respectively. Therefore, the mechanism for the reaction of BrHg + O_2 should be described by the equilibrium process

$$BrHg + O_2 \rightleftharpoons BrHgOO$$
 (R2)

Given the abundance of O_2 in the atmosphere and the uncertainty in the bond energy, we think it is necessary to study this reaction experimentally and computationally. We report on our combined experimental and theoretical studies of the reaction R2 and discuss the atmospheric impact of reaction R2 and BrHgOO as an intermediate on mercury redox chemistry, as well as the challenges for experimental measurement using LIF spectroscopy due to fluorescence quenching of BrHg by O_2 .

II. METHODS AND MATERIALS

II.I. Experimental Methods. The photolytic precursor of the BrHg radical, mercury(II) bromide (HgBr₂), vapor was generated by heating HgBr₂ powder (Acros Organics, 99+%) to 305 K in a flow tube, and transferred to the reactor by N₂ gas (Airgas, 99.999%). ⁴⁶ The HgBr₂ concentration was 6 × 10¹² molecule cm⁻³, extrapolated from the literature data⁴⁷ using the Clausius-Clapeyron equation. NO gas (Airgas, 2534 ppm in N_2 with the NIST-certified accuracy of $\leq 1\%$) was purified using an Ascarite trap (Sigma-Aldrich)⁴⁸ and characterized by UV-vis spectroscopy. 49 The absence of impurities, e.g., NO2, was verified by capturing the UV-vis absorption spectrum of the gas mixture from 192 to 660 nm. [NO₂] is estimated to be <2% of [NO] even without using an Ascarite trap. The measured rate constants of BrHg + NO varied only by <8% (within the experimental uncertainty) with or without an Ascarite trap inserted in the gas line, which shows an insignificant impact by NO₂. NO and O₂ were diluted in N₂ before being transferred to the reactor.

The laser photolysis—laser-induced fluorescence (LP-LIF) apparatus is shown in Figure 1 and is similar to the one used in our previous work. 10,17 Therefore, the experimental setup is described briefly here. BrHg radicals were generated from photolysis of HgBr₂ at 266 nm using an Nd:YAG laser (Spectra-Physics PRO-350, energy flux of <127 mJ pulse⁻¹ cm⁻² at the reaction region). BrHg was probed by a dye laser (Radiant NarrowScan, linewidth ~0.05 cm⁻¹, at ~256 nm, ~10 μ J) that was pumped by another Nd:YAG laser (Continuum Powerlite 8020, at 355 nm). The ($\tilde{D}^2\Pi_{3/2}$, v'=2) $\leftarrow (\tilde{X}^2\sum^+$, v''=0) transition at 255.97 nm was used to probe the BrHg radicals.
The intensity of a small fraction of the probe laser was measured by a photodiode (Thorlabs DET 210) to normalize the LIF signal at each laser shot. The

photolysis beam and the probe laser were focused at the center of the reactor to maximize BrHg generation and the LIF intensity and intersect each other at a sharp acute angle of $\sim\!11^\circ$. The resulting fluorescence emissions from the excited radicals were detected orthogonally to the two laser beams by a photomultiplier tube (PMT, Hamamatsu R7400U-03). The LIF signal around 500 nm from the $\tilde{B}^2 \sum_{1/2}^+ \to \tilde{X}^2 \sum^+$ transition was found to be stronger than that around 260 nm from the $\tilde{D}^2 \Pi_{3/2} \to \tilde{X}^2 \sum^+$ transition, so the PMT was screened with a 500 \pm 20-nm band-pass filter to detect the fluorescence from the $\tilde{B}^2 \sum_{1/2}^+ \to \tilde{X}^2 \sum^+$ transition.

The PMT signal was amplified (ORTEC 9305) and transmitted to a boxcar system (Stanford Research System SR250) before feeding into the in-house-developed data acquisition software. The delay time between the photolysis laser and the probe laser was controlled by a digital delay (Stanford Research System DG 535) and automatically scanned from 1 to 1000 μ s depending on experimental conditions. Normalized LIF signals were averaged over 10–20 laser shots at each delay time. The change in the LIF signal as a function of delay time was used to determine the rate of BrHg radical disappearance in the reaction with NO or O₂. A 20-point scan of the delay time for one experiment condition typically took <60 s, which minimized the uncertainty due to the fluctuations in the photolysis laser energy.

The reactor was made of a six-way CF port cross stainless steel high-vacuum chamber (MDC) that consists of three perpendicular axes. One axis at the horizontal plane was used for the laser beams passing through, one also at the horizontal plane for the gas mixtures flowing, and one axis at the vertical plane for the LIF detection. The flow rate was regulated by mass flow controllers (MFC, Parker 601CVNAAD22V; Alicat MCS-5SLPM-D) with a total flow rate of 0.97-13.66 SLPM and a short residence time of 1.4 s in the reactor. Gas flow rate/residence time was varied to investigate the influence of side reactions. The reactor and gas-flow tubes were jacketed and insulated, and their temperature was controlled (MDC BDTC-K-120) at 315-353 K, at least 10 K higher than the HgBr₂ reservoir to prevent vapor condensation. The temperature and the pressure in the reaction region were measured by a calibrated thermocouple (Omega) and a calibrated manometer (MKS 626A13TAE, 1-1000 Torr), respectively. The deviation between the actual pressure and the nominal pressure reported was ~5-8 Torr, depending on the experimental conditions. Experiments at low pressures such as 50 Torr usually have higher uncertainty (up to 10%) due to greater difficulty in stabilizing the pressure in the dynamic flow experimental setting.

The concentration of BrHg radicals in the experiments was estimated to be $\sim\!\!2\times10^{11}$ molecule cm $^{-3}$ based on the absorption cross section of HgBr $_2$ at 266 nm ($\sim\!\!7\times10^{-19}$ cm 2) 27,52 and the HgBr $_2$ concentration in our experiment setting (3.0 \times 10 12 molecule cm $^{-3}$), 47 and the BrHg quantum yield ($\sim\!\!0.6$). 24 The concentrations of NO and O $_2$ were derived from the mole fraction based on the ratio of their flow rates to the total flow rate and were set to be (3.5–30.8) \times 10 14 and (1.2–4.9) \times 10 17 molecule cm $^{-3}$, respectively, to establish pseudo-first-order conditions and mitigate side reactions.

II.II. Computational Methods. All calculations presented in this article were carried out using a combination of basis sets. Dunning's augmented correlation-consistent triple- ζ basis sets (aug-cc-pVTZ)^{53,54} was used for oxygen and nitrogen atoms. Energy-consistent pseudopotentials (PP) represented

the 60 innermost electrons of Hg (ECP60MDF) and the 10 innermost electrons of Br (ECP10MDF), 55,56 while the aug-cc-pVTZ-PP⁵⁷ basis set was used for the explicitly treated electrons. This combination of basis sets is denoted below as AVTZ. The frozen-core approximation was applied to the first 8 and 18 explicitly treated electrons of Hg and Br, respectively, when post-Hartree—Fock methods were used. The AVTZ basis set was selected based on the reliability offered by the combination of augmented correlation-consistent Dunning-type basis sets with the pseudopotentials implemented by Stuttgart/Cologne group. This type of basis sets allow inclusion of scalar relativistic effects arising from the innermost electrons of Hg and Br atoms while at the same time offering the flexibility provided by a polarized triple- ζ basis set and the addition of diffuse functions.

The reactants and products were fully optimized at coupledcluster singles and doubles with the perturbative triples (CCSD(T)) method, 58,59 followed by frequency calculations at the same level of theory in ORCA program 5.0.1.60 The gradients and Hessians were fully calculated using two-sided numerical differentiation. To study the energy profiles, we performed relaxed scans at the DFT level, which involves energy calculations at short, equilibrium, and long distances. A good option to evaluate the interactions between the electron clouds of reactants at longer ranges is the use of dispersion corrections, long-range corrected functionals, or a combination of both. Therefore, for BrHgNO, the topography of the potential energy surface (PES) of the ground state along the reaction coordinate $d_{\rm BrN}$ (Br-N distance) was studied using relaxed scans at B97D3^{61,62} in Gaussian 16.⁶³ For BrHgOO, the $d_{\rm HgO}$ (Hg-O distance) was scanned using ORCA and the CAM-B3LYP⁶⁴ and ω B97X⁶⁵ functionals, including the D3BJ^{62,66} empirical dispersion correction. In cases where we only estimated the enthalpy for other reactions (energies at equilibrium geometries), we used PBE0 hybrid functional as a rapid alternative to estimate the enthalpy change, given that it has been shown to provide good bond energies on Hg derivatives at a low computational cost. 18 The scans were carried out after obtaining the most stable wavefunctions within the unrestricted approach. Then, the highly correlated CCSD(T) method was used for single points along the geometries obtained from the scans. In addition, in the case of BrHgNO, the complete active space self-consistent field (CASSCF) method⁶⁷ was used to generate the reference wavefunction as a full configuration interaction expansion in an active space composed of 10 electrons in 8 orbitals (see Figure S1 in the Supporting Information), leading to a configuration space formed by 784 configuration state functions for singlets. State-specific (SS) and state-average (SA) calculations were performed for the lowest two singlets and two triplets. Then, strongly contracted N-electron valence state second-order perturbation theory (SC-NEVPT2)⁶⁸⁻⁷¹ was used to take the dynamic electron correlation into account. Standard and quasidegenerated (QD) NEVPT2 energies were evaluated to take possible interactions of the states into account. The QD-NEVPT2 approach⁷² uses a multidimensional reference space and constructs an effective Hamiltonian, which is computed perturbatively, allowing the CASSCF states to interact via nondiagonal terms. The spin-orbit coupling was calculated along the path by calculating the matrix elements of the spinorbit Hamiltonian (\hat{H}^{SO}) , and its diagonalization led to mixed states.

To get zero-point energy (ZPE) and Gibbs free energies corrections ($G_{\rm corr}$), frequency calculations were performed at the corresponding DFT level at each point along the scans. Free energy corrections ($G_{\rm corr}$) were obtained at different temperatures. Then, the free energy (G) along each point of the paths was calculated by adding $G_{\rm corr}$ to the energy ($E_{\rm elec}$) from CCSD(T) (for BrHgOO) or NEVPT2 (for BrHgNO). The normal modes and the ZPE-corrected energy of the maximum along the free energy paths (ΔG^{\ddagger}) were used in the thermo program from the MultiWell Program Suite $^{73-75}$ to estimate the rate constants at 200, 220, 240, 260, 280, 298.15, 313, 323, 353, and 373 K through the canonical transition state theory (CTST) implemented in the MultiWell Program Suite. $^{73-75}$ The minimum value of the CTST rate constant, $k_{\rm CTST}(T)$, along the path corresponds to the variational transition state theory (VTST) rate constant, $k_{\rm VTST}(T)$.

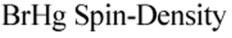
We used Rice–Ramsperger–Kassel–Marcus (RRKM) theory/Master Equation calculations in MultiWell^{73–75} to compute $k_2([M], T)$, where [M] is the total concentration of gas-phase molecules, i.e., N_2 in this study. Lennard-Jones parameters for N_2 are $\sigma=3.70$ Å and $\varepsilon/K=85$; for BrHgOO, we used $\sigma=5.0$ Å and $\varepsilon/K=700$. Energy transfer was modeled as a single exponential with $\alpha=100$ cm⁻¹. MultiWell simulations were carried out at 200–333 K and [M] of 2.5×10^{16} – 2.5×10^{19} molecule cm⁻³. The Lindemann mechanism was applied to the reaction of BrHg + O_2

$$\begin{array}{l} \text{BrHg} + \text{O}_2 \xrightarrow{k_2^{\infty}(T)} \text{BrHgOO}^* \\ \\ \text{BrHgOO}^* \xrightarrow{k_{-2}(E)} \text{BrHg} + \text{O}_2 \\ \\ \text{BrHgOO}^* + \text{N}_2 \xrightarrow{k_{\text{quench}}([M]), T} \text{BrHgOO} + \text{N}_2 \end{array}$$

where $k_2^{\infty}(T)$, $k_{-2}(E)$, and $k_{\text{quench}}([M], T)$ represent the rate constant for the formation of activated BrHgOO, i.e., BrHgOO* (which equals $k_2(T)$ in the high-pressure limit), for the dissociation of BrHgOO*, and for the collisional quenching of BrHgOO*, respectively. We initiated simulations with BrHgOO* populated from BrHg + O₂, from which we determined the fraction of BrHgOO* that was quenched to thermalized BrHgOO, $f_{\text{quench}}([M], T)$. The number of Monte Carlo trials was adjusted to achieve <5% statistical uncertainty in f_{quench} at all T and [M]. $k_2([M], T)$ was determined as $f_{\text{quench}}([M], T) \times k_2^{\infty}(T)$. A preliminary investigation of reactions of BrHgOO with the atmospheric radicals, i.e., NO, NO₂, and HOO, was conducted in this study. This investigation applied the PBE0 functional with the AVTZ basis set, a combination that has proven to provide a reliable guide to BrHg chemistry in our previous investigations. 16,19

III. RESULTS AND DISCUSSION

According to the CCSD(T) and CASSCF calculations, the BrHg radical (doublet) possesses an electronic structure characterized by a delocalized unpaired electron that leads to an almost equally distributed spin-density on Br and Hg atoms (Figure 2). This explains why BrHg can react with radicals, Y (such as Br and NO₂), to either reduce $Hg^{(I)}$ to $Hg^{(0)} + BrY$ or oxidize $Hg^{(I)}$ to $Hg^{(II)}$ as BrHgY, as discussed in Section I. It seems that the products of BrHg reactions should strongly depend on the orientation of the molecular collisions with other radicals or species such as O_2 . If the collision occurs between Hg atom and another radical center, the reaction can easily proceed toward the oxidation process to $Hg^{(II)}$; however,



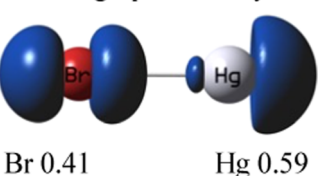


Figure 2. Spin-density based on Mulliken population analysis from CCSD(T)/AVTZ calculation using linearized density from CCSD(T). The spin densities were confirmed by the orbital-optimized coupled-cluster doubles (OOCCD) method.

when the radical collides with the Br atom, a reduction reaction to $Hg^{(0)}$ takes place.

III.I. Rate Constants of BrHg + NO. III.I. Experimental Results. The temporal disappearance of [BrHg] should be well expressed by a single-exponential decay under pseudo-first-order conditions, as in eq 1

$$\ln\left(\frac{[\text{BrHg}]_t}{[\text{BrHg}]_0}\right) = -k_1' t \tag{1}$$

where k'_1 is the pseudo-first-order rate constant for the disappearance of BrHg that follows eq 2

$$k_1' = k_1[NO] + k_{other}$$
 (2)

where k_1 is the second-order rate constant for the reaction of BrHg + NO, and $k_{\rm other}$ is the effective rate constant for other loss processes such as side reactions and diffusion.

Figure 3a shows typical plots of the natural logarithm of BrHg LIF intensity versus the delay time between the photolysis laser and the probe laser at different [NO]; data is shown at five different [NO] along with their weighted linear fits. The absolute values of the slopes of these linear fits, i.e., the pseudo-first-order rate constant k'_1 , are plotted against the corresponding [NO] to obtain the second-order rate constants, k_1 , as shown in Figure 3b. Values of k'_1 under different experimental conditions are listed in Tables S1 and S2.

The data in Figure 3a,b exhibit the high linearity expected from pseudo-first-order conditions with $R^2 > 0.96$ and ≥ 0.995 , respectively. The nonzero y-intercepts can be interpreted as the sum of the pseudo-first-order rate constants from all loss processes other than the reaction with NO. The pseudo-firstorder rate constants k'_1 at [NO] = 0, measured to assess those loss processes, are included in the linear least-square fits. Excluding the data points in the absence of NO in the linear fits affects the resulting slope by less than $\pm 8\%$, which is well within the uncertainty of the rate constant measurement. This suggests minimal loss of BrHg results from side reactions with species relevant to NO gas, such as BrNO, BrHgO, and NO2, but that loss arises, instead, from diffusion and side reactions with species such as BrHg and Br. In selected experiments, by increasing the total gas flow rate to decrease the residence time from 1.4 to 0.6 s at 150-700 Torr and 315 K, the resulting rate constants are affected by less than 11%, which is within the uncertainty of the rate constant measurement. This suggests the accumulation of photolytically produced species from multiple laser shots does not occur to a significant extent, probably due to the diffusion of the unwanted species out of the photolysis region ($\leq 0.5\%$ of the reactor volume).

The measured absolute rate constants k_1 at different temperatures and pressures over the range 315–353 K and

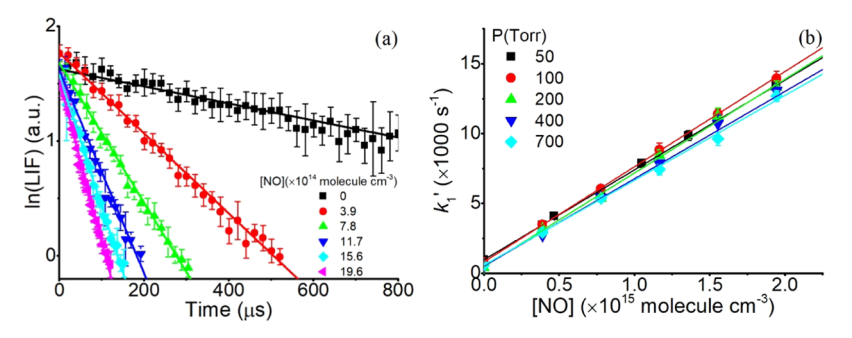


Figure 3. (a) Typical linear decays of $\ln(\text{LIF})$ as a function of the decay time (between the photolysis laser and the probe laser) for the reaction of BrHg with NO at different [NO] at 100 Torr and 315 K. Straight lines represent weighted linear fits. Error bars are 1σ of the average over 10 normalized LIF signals. (b) Typical plots of the pseudo-first-order rate constant, k'_{1} , for BrHg + NO versus [NO] at different pressures (at 315 K) with weighted linear fits. Error bars are 2σ of the fitted slopes of $\ln(\text{LIF})$ decays.

50-700 Torr are listed in Table 1 and displayed in Figure 4. The rate constant exhibits no pressure and temperature

Table 1. Second-Order Rate Constants $k_1(p, T)$ for BrHg + NO with Error Bars of 2σ

$k_1 \ (\times 10^{-12} \ \text{cm}^3 \ \text{molecule}^{-1} \ \text{s}^{-1})$				
	315 K	323 K	333 K	353 K
50 Torr	6.43 ± 0.16	7.43 ± 1.36	7.43 ± 1.02	8.24 ± 0.31
100 Torr	6.93 ± 0.39	7.17 ± 1.08	7.12 ± 0.28	7.32 ± 0.59
200 Torr	6.70 ± 0.32	6.66 ± 0.24	7.36 ± 0.27	6.81 ± 0.66
400 Torr	6.27 ± 0.45	6.63 ± 0.34	6.85 ± 0.11	6.88 ± 0.21
700 Torr	6.08 ± 0.21	6.68 ± 0.31	6.66 ± 0.15	6.45 ± 0.22

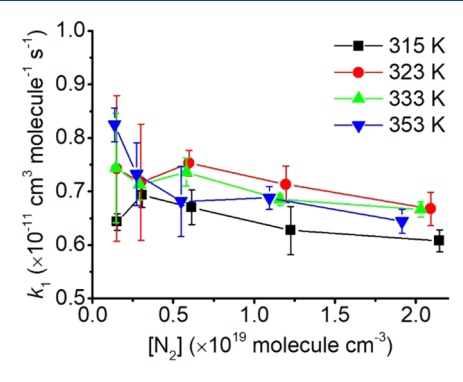


Figure 4. Measured rate constant k_1 of BrHg + NO versus $[N_2]$ at 315, 323, 333, and 353 K. Error bars represent 2σ of the fitted slopes of k'_1 versus [NO].

dependence under experimental conditions. The measured rate constants at 50 Torr usually have larger uncertainties than the others, mainly due to the greater difficulty in maintaining the pressure with minimal fluctuation (<10%) at low pressure, resulting in greater uncertainty of [NO] determination. The average of the rate constants listed in Table 1 is $7.0^{+1.3}_{-0.9} \times 10^{-12}$ cm³ molecule $^{-1}$ s $^{-1}$, which can be used as the overall rate constant over the range 315–353 K and 50–700 Torr.

The lack of pressure dependence of the measured rate constants for BrHg + NO suggests that this reaction may not lead to recombination. Dibble et al. reported that the bond energy of BrHg–NO is sufficiently small (12 kcal mol⁻¹)^{13,14} such that BrHgNO would dissociate rapidly in the experiment. Assuming the Arrhenius pre-exponential A for the dissociation is as low as 1×10^{13} s⁻¹, BrHgNO has a lifetime as short as 1.4 μ s at 315 K. The reaction BrHg + NO \rightleftharpoons BrHgNO would reach equilibrium in less than 10 μ s at 315 K, yet Figure 3a

shows that single-exponential decay of the BrHg signal extends out to hundreds of μ s at 315 K. Instead of the association reaction to form BrHgNO, the temperature- and pressure-independence of k_1 is more consistent with a barrierless disproportionation reaction forming Hg + BrNO (reaction R1). This could occur if the N atom of NO approaches the Br of BrHg. The rate constant of reaction R1 may be considered nearly pressure-independent under our experimental conditions, analogous to the reaction of BrHg + NO₂ \rightarrow Hg + BrNO₂. Both reactions correspond to the reduction of mercury from Hg⁽¹⁾ to Hg⁽⁰⁾. The lack of temperature dependence of the measured rate constant indicates that the reaction R1 could be barrierless. The computational results presented immediately below are consistent with the absence of a barrier.

III.I.II. Computational Results. The unpaired electron of the NO radical can be on the two equivalent singly-occupied molecular orbitals (SOMOs) $\pi^*_{1,NO}$ or $\pi^*_{2,NO}$ (see Figure S1); however, as BrHg approaches along the axis of $\pi^*_{1,NO}$, the degeneracy is lost and the lower-energy doublet is described by the unpaired electron on $\pi 1,NO^*$. At long d_{BrN} distances, the wave function is described by an open-shell configuration, which gradually becomes a closed shell as d_{BrN} approaches the equilibrium distance.

The ZPE-corrected energy profiles at B97D3 and CAM-B3LYP-D3BJ for the reduction reaction show a barrierless potential energy surface along the reaction coordinate, whose minimum is a final complex (FC) that is expected to be vibrationally excited and should rapidly dissociate to BrNO and $\mathrm{Hg}^{(0)}$. The inclusion of electron correlation via single points at CCSD(T) and the subsequent addition of the ZPE corrections from B97D3 show a barrier of 2.4 kcal mol⁻¹. This barrier is likely an artifact, as is often observed at CCSD(T) along the barrierless reaction path for two radicals forming singlet products (see Figure S2). 77,78 According to CCSD(T) calculations, $\Delta H_r^{\circ}(0 \text{ K})$ and ΔG_r° (298 K) for the reduction reaction (forming BrNO and Hg) are -13.4 and -0.5 kcal mol⁻¹, respectively. For the oxidation reaction (forming BrHgNO), $\Delta H_{\rm r}^{\circ}(0~{\rm K})$ and $\Delta G_{\rm r}^{\circ}$ (298 K) are -11.9 and -2.4 kcal mol⁻¹, respectively. When the energy profile is built using QD-NEVPT2 electronic energies, there is an initial baseline of 0.37 kcal mol⁻¹ at very long distances (Figure S2a). The nature of the wavefunction along the path acquires an important multiconfigurational character, where in the range from 2.75 to 2.95 Å, the wavefunctions are mainly described by three configurations with weights of 0.40, 0.39, and 0.12. The barrier shown on the CCSD(T) profiles is located at 2.85 Å,

which is within this range. From this point on, we are going to discuss the results from QD-NEVPT2, given that it can better describe the multiconfigurational character of the wavefunction during bond-breaking and formation. The reaction coordinate is mostly defined by the $d_{\rm BrN}$ and $d_{\rm BrHg}$ distances, as shown in Figure 5. The $d_{\rm BrN}$ distance dominates the reaction that forms

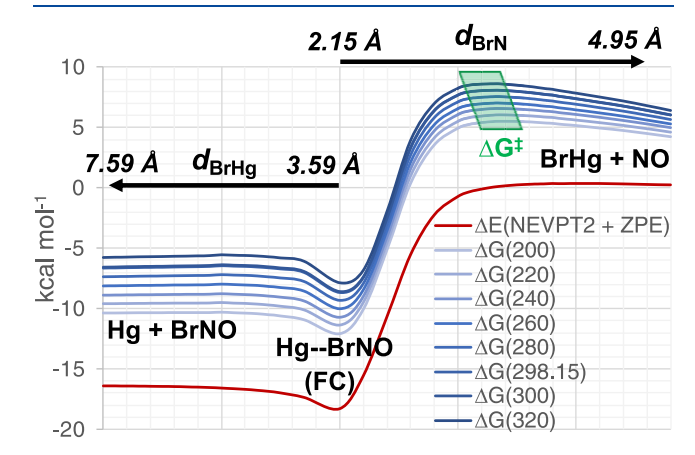


Figure 5. Energy profiles (kcal mol⁻¹) along the $d_{\rm BrN}$ and $d_{\rm BrHg}$ distances. Energies have been calculated with respect to the reactants separated at infinite distance. $G = E_{\rm elec}^{\rm (QD-NEVPT2)} + G_{\rm corr}^{\rm B97D3}$; $E = E_{\rm elec}^{\rm (QD-NEVPT2)} + {\rm ZPE}^{\rm B97D3}$.

the final complex (Hg–BrNO) from BrHg and NO. The $d_{\rm BrHg}$ distance dominates the formation of separated products (Hg and BrNO) from Hg–BrNO. This complex is ~18 kcal mol⁻¹ lower than reactants, and it is characterized by $d_{\rm BrN} = 2.15$ Å and $d_{\rm BrHg} = 3.59$ Å.

The free energy surface has a barrier from reactants to the exit channel complex, and it gets displaced to slightly shorter $d_{\rm BrN}$ as the temperature increases. The free energy barrier, ΔG^{\ddagger} , at QD-NEVPT2//B97D3, at 200 K, is 5.5 kcal mol⁻¹ and it is located at $d_{\rm BrN}=3.55$ Å, whereas at 320 K, this barrier becomes 8.6 kcal mol⁻¹ with $d_{\rm BrN}=3.45$ Å. At 298.15 K, ΔG^{\ddagger} is 7.5 kcal mol⁻¹. As can be seen from Figure 6, the computed rate constant for the reduction reaction varies only modestly with temperature (less than a factor of 3 in the range 200 K \leq $T \leq 360$ K), and this weak temperature dependence agrees qualitatively with the experimental results shown in Figure 6b. The calculated rate constant is ~12 times smaller than the experimental value, a level of error that is unfortunate, but not surprising, given the sources of uncertainties: computing NEVPT2 energies with B97D3 geometries, the use of B97D3

for thermal corrections, and the fact that NEVPT2 only includes dynamic electron correlation to second order.

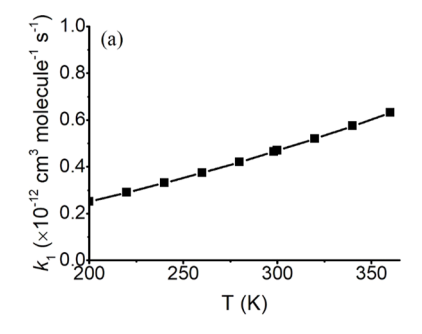
III.II. Kinetics Study of BrHg + O₂. |||.||.|. Experimental Results. We studied BrHg temporal behavior in the presence of a high O_2 concentration of $(1.2-4.9) \times 10^{17}$ molecule cm⁻³ and determined the pseudo-first-order rate constant k'_2 at 333 K and 85 \pm 5 Torr. Figure 7 shows that k_2 does not depend on [O₂]. This suggests that the observed loss of BrHg is not due to the reaction with O2 but to diffusion out of the reaction zone and/or side reactions. In terms of the BrHg + O2 reaction, there are two likely interpretations. One is that the BrHg + O₂ reaction reaches equilibrium before we obtain the first one or two BrHg LIF signals (10-20 µs), but our computational simulations suggest otherwise (see computational discussion below). The other explanation is that the reaction of BrHg with O_2 is negligible on the ~ 1 ms time scale of the experiment. If we assume that no more than 50% of the observed k'_2 in Figure 7b is due to BrHg reaction with O_2 , this would imply a rate constant of $<2.4 \times 10^{-16} \text{ cm}^3 \text{ molecule}^{-1}$ s⁻¹ (considering the highest [O₂] used), which is much higher than our computational results $(4.2 \times 10^{-19} \text{ cm}^3 \text{ molecule}^{-1}$ s⁻¹; listed in Table S5).

An increase in $[O_2]$ above those used here would enable us to gain more insight into the rate constant. Unfortunately, this is not possible in the present experiment because O_2 efficiently quenches the fluorescence of $BrHg(\tilde{B}^2\sum_{1/2}^+)$. This is evident from the decrease of the initial LIF signal (at $20~\mu s$) with the increase of $[O_2]$, as shown in Figure 7a. We measured the fluorescence lifetime of the excited state $BrHg(\tilde{B}^2\sum_{1/2}^+)$ by capturing its fluorescence intensity in a 400 MHz oscilloscope as a function of time, starting right after the excitation light was switched off. The fluorescence intensity decays exponentially with the excited state population of $BrHg(\tilde{B}^2\sum_{1/2}^+)$ at the rate that follows the Stern–Volmer relationship⁷⁹

$$k_{\rm f} + k_{\rm nf} + k_{\rm q}[O_2] = 1/\tau_0 + k_{\rm q}[O_2] = 1/\tau_{\rm q}$$
 (3)

where $k_{\rm f}$ $k_{\rm nf}$ and $k_{\rm g}$ represent the rate constant of the radiative decay for BrHg($\tilde{\rm B}$), the total rate constant of first-order processes that do not lead to fluorescence, such as nonradiative deactivation and internal conversion, and the rate constant of fluorescence quenching by O₂, respectively. $\tau_{\rm q}$ and $\tau_{\rm 0}$ are the lifetimes of the $\tilde{\rm B}$ state with and without the quencher, respectively.

Figure 8a shows decent linear decays in the plots of the natural logarithm of the fluorescence intensity versus time with R^2 of >0.968; the slopes of such linear fits produce the reciprocals of the fluorescence lifetimes of the excited BrHg(\tilde{B}) state at different $[O_2]$. Figure 8b exhibits a typical Stern—



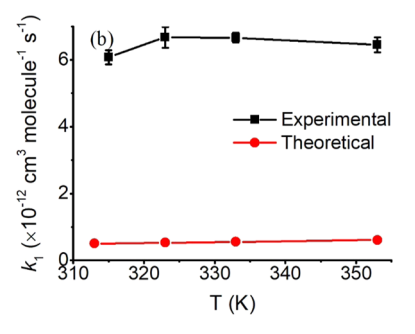


Figure 6. (a) Calculated rate constants (k_1) based on CTST at different temperatures ranging from 200 to 360 K. (b) Experimental (at 700 Torr with error bars of 2σ) and computational rate constants (k_1) at 313, 315, 323, 333, and 353 K.

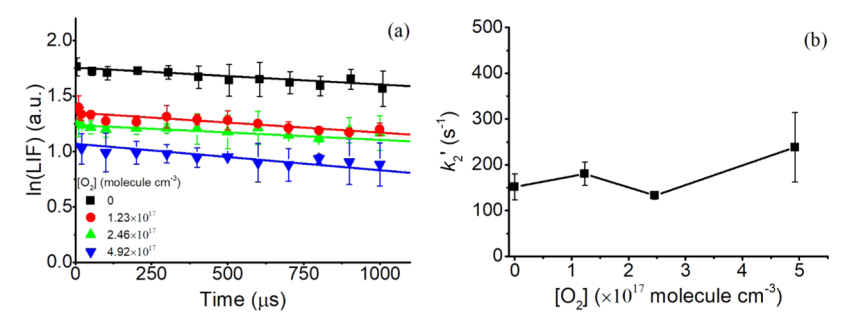


Figure 7. (a) Typical linear decays of $\ln(\text{LIF})$ versus the decay time for $\text{BrHg} + \text{O}_2$ reactions at 85 ± 5 Torr and 333 K; error bars are 1σ of the average over 100-200 LIF signals. (b) Plots of k_2' versus $[\text{O}_2]$ at 333 K. Error bars are 1σ of the fitted slopes of $\ln(\text{LIF})$ decays in (a).

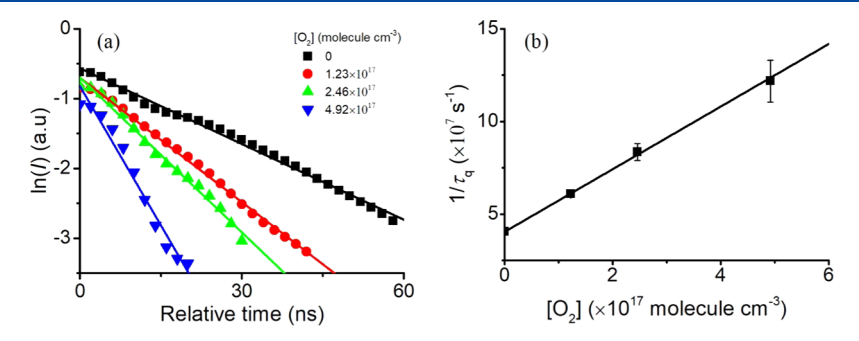


Figure 8. (a) Linear decays of $\ln(I)$ versus time at different $[O_2]$, where I is the intensity of the fluorescence emission from the $\tilde{B}^2\sum_{1/2}^+ \to \tilde{X}^2\sum_{1/2}^+$ transition right after switching off the excitation laser. (b) Stern-Volmer plot for the LIF quenching of BrHg by O_2 with a weighted linear fit to eq 3. The error bars represent 2σ statistical error.

Volmer plot using the fluorescence lifetimes at different [O₂] with an R^2 of 0.9988. The fluorescence lifetime of the B state in the absence of O₂, τ_0 , is 24.8 \pm 0.6 ns derived from the yintercept of Figure 8b, which is close to the previously reported data (measured to be 23.2 ± 0.5 ns). The rate coefficient, $k_{q\gamma}$ for the BrHg(\tilde{B}) quenching process by O_2 at 333 K, is determined to be $(1.7 \pm 0.1) \times 10^{-10}$ cm³ molecule⁻¹ s⁻¹ from the slope of the linear fit in Figure 8b. This is slightly higher than the previously reported one by a factor of 1.8, which is acceptable considering the uncertainty of this type of experiments (typically within a factor of 2 based on the survey of the literature).81 The fluorescence quenching by undissociated parent species HgBr₂ and its photofragments (BrHg*, BrHg, Br and Hg), bath gas N2, and the impurity gases, are possible contributing factors, but their impacts are modest due to their low concentrations (such as HgBr₂) or low quenching rates (such as N_2 with a quenching rate of $\leq 1.5 \times 10^{-13}$ cm³ molecule⁻¹ s⁻¹). 81,82 The thermodynamic threshold for O₂ photolysis is 242 nm (at 0 K), and O₂ has an extremely small collision-induced absorption cross section at 256 and 266 nm $(<0.05 \times 10^{-24} \text{ cm}^2)$; 45,83 therefore, photodissociation and excitation of O2 should not be a concern in this experiment. The origin of the discrepancy needs further investigation.

If the equilibrium is established before the first measurement takes place at 20 μ s, BrHg + O₂ \rightleftharpoons BrHgOO can be also responsible for the decrease of [BrHg(\tilde{X})] (thus the LIF signal). However, Figure 9 shows that the measured BrHg fluorescence intensities in the kinetics experiments at a delay of 20 μ s are close to those predicted from the Stern–Volmer relationship. This means the formation of BrHgOO does not contribute significantly to reducing the LIF signal in the kinetic experiments. Instead, this finding supports the interpretation that the reaction BrHg + O₂ \rightleftharpoons BrHgOO either has a very

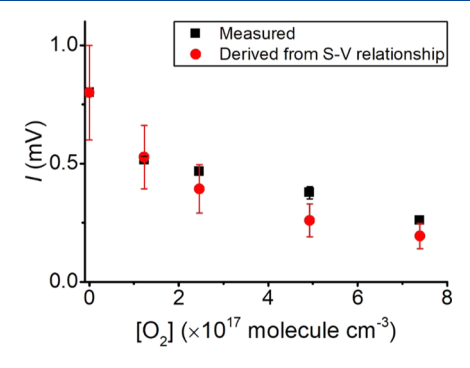


Figure 9. Plot of BrHg fluorescence intensities versus $[O_2]$. Experimental data measured at 20 μ s is shown in black, where error bars are 1σ of the average over 100-200 LIF signals. Predicted values from the Stern–Volmer relationship using the τ_0 and k_q from this work are shown in red, with the error bars computed from error propagation.

small equilibrium constant or reaches equilibrium only after times much longer than those for our experiment.

The excited state $\operatorname{BrHg}(\tilde{B})$ may follow several kinetics pathways in the presence of O_2 : nonradiative relaxation from \tilde{B} to \tilde{X} resulting from energy transfer between $\operatorname{BrHg}(\tilde{B})$ and O_2 (reaction R3), and reactive dissociation (reactions R4 and R5), ⁸¹ as shown in Figure 10. In the case of the energy transfer process R3, O_2 may be excited to the Herzberg II forbidden system $(\tilde{c}^1\sum_u^1-\tilde{X}^3\sum_g^-)$, ⁸⁴ as some emission bands such as the progression of (0-8), (0-9), and (0-10) are located in the spectral range of 480–507 nm that could lead to resonance in the energy transfer process between $\operatorname{BrHg}(\tilde{B})$ and O_2 . There is no existing study on the reactions of the excited state $\operatorname{BrHg}(\tilde{B})$ with O_2 (reactions R4 and R5). However, we know reaction R4 is exothermic by 51 kcal mol^{-1} , as D_0 for $\operatorname{BrHg}(\tilde{X})^{45}$ is only ~ 16 kcal mol^{-1} and T_e for $\operatorname{BrHg}(\tilde{B}^2\sum_{1/2}^+)$ is 23 485 cm⁻¹ (67.1

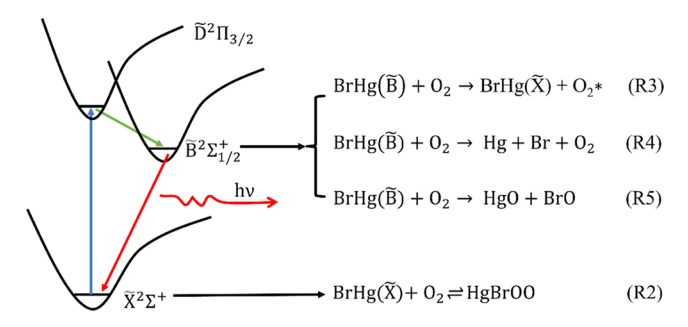


Figure 10. Excitation scheme for the LIF of BrHg along with possible kinetics pathways for BrHg(\tilde{B}) and BrHg(\tilde{X}). The excitation transition is at ~256 nm, with subsequent fluorescence transition near 500 nm.

kcal mol⁻¹). ⁸⁵ Reaction R5 appears to be endothermic by 8 \pm 5 kcal mol⁻¹. Thus, reaction R5 is unlikely to decrease the BrHg fluorescence, but reaction R4 is feasible. Similar processes may remove BrHg(\tilde{D}) (the source of BrHg(\tilde{B}) in our experiment), which would further reduce the LIF signals. To study the reaction of BrHg(X) + O₂ at high [O₂], a different approach, such as cavity ringdown spectroscopy, is needed to quantify and track absolute [BrHg(\tilde{X})] without the issue of fluorescence quenching.

III.II.II. Computational Results. According to the ZPEcorrected CCSD(T) energies at 0 K, the product (BrHgOO) from oxidation of BrHg by O₂ is 7.2 kcal mol⁻¹ lower than reactants, whereas the BrOO and Hg obtained from the reduction reaction are 15.2 kcal mol⁻¹ higher than reactants. The endothermicity of forming BrOO + Hg leads to rate constants far too low to occur in the atmosphere or in our experiments. Scanning the approach of O2 to BrHg, we were surprised to find a barrier to reaction, albeit a small one (see Figure 11). Our CCSD(T) geometry optimizations confirmed the CAM-B3LYP-D3BI and ω B97X-D3BI results. According to the three different methods used, this barrier on the ZPEcorrected energy profiles is between 0.6 and 2.6 kcal mol⁻¹, with the highest value obtained with CCSD(T) and the lowest value at CAM-B3LYP-D3BJ level, as shown in Figure 11a. CCSD(T) relative energies with a triple- ζ basis set commonly show errors of 1–2 kcal mol⁻¹, and DFT with a triple- ζ basis set exhibits larger uncertainties. So the three model chemistries used here agree well by the standards of quantum chemical calculations, although the resulting variation in the rate constant will be high by the standards of the experiment.

The transition state has only modest multireference character, as the T_1 diagnostic is only 0.026 (see Figure S3).

At CCSD(T), the equilibrium constant, K_c , for the formation of BrHgOO, can be represented as 1.4×10^{-26} e^{+3650/T} cm³ molecule⁻¹, corresponding to 7×10^{-22} cm³ molecule⁻¹ at the 333 K temperature of our experiments. Compared to the CCSD(T) values over the range $200 \le T \le 373$ K, K_c at ω B97X-D3BJ are higher by a factor of 4–20, and K_c at CAM-B3LYP-D3BJ are lower by a factor of 2.6–5.9 (see Table S3).

The Gibbs free energy profiles at 298 K show maxima of 11.5, 10.1, and 9.4 kcal mol⁻¹ with respect to separated reactants at CCSD(T)/ ω B97X-D3BJ, ω B97X-D3BJ, and CAM-B3LYP-D3BJ, respectively, as shown in Figure 11b. The positions of these maxima define the variational transition state for each theoretical method and are used to compute rate constants with VTST. The variational transition state has d_{HgO} = 2.473 Å at all temperatures and levels of theory used. The rate constants $k_2(T)$ for the formation of BrHgOO were estimated along with the equilibrium constant $K_c(T)$. Then, the rate constant for the dissociation reaction $k_{-2}(T)$ was calculated as $k_2(T)/K_c(T)$. Figure 12 illustrates the temperature dependence of $K_c(T)$ and $k_2(T)$, and the values are listed in Table S3. Note that, because of the barrier to reaction, the rate constant for this association reaction has a positive temperature dependence. Arrhenius pre-exponential factors are derived in Figure S5.

The rate constants computed from VTST are in the high-pressure limit, but the low BrHg–OO bond energy argues for the actual rate constants being closer to the low-pressure limit. At the experimental conditions of 333 K and 85 Torr, $k_2 = 4.2 \times 10^{-19}$ cm³ molecule⁻¹ s⁻¹. Given the range of [O₂] used in our experiments, the pseudo-first-order rate constant, k_2 for loss of BrHg in reaction with O₂ ranged from 0.05 to 0.2 s⁻¹. Based on these results, loss of BrHg from reaction with O₂ was negligibly small over the times monitored in the experiments. As a sensitivity test, we increased D_0 for BrHg–OO by 2 kcal mol⁻¹, increasing $K_c(333 \text{ K})$ by a factor of 21. This only increased k_2 by a factor of 5, confirming the conclusion that the reaction with O₂ could not account for the observed losses of BrHg in our experiments.

Table S4 presents the values of k_2 versus T and [M]. k_2 was at or very near the low-pressure limit for $[M] \le 2.5 \times 10^{18}$ molecule cm⁻³ at all temperatures. We did not attempt to fit $k_2([M], T)$ to the Troe expression ^{86,87} because the maximum deviation from the low-pressure limit was only 17% (at 200 K).

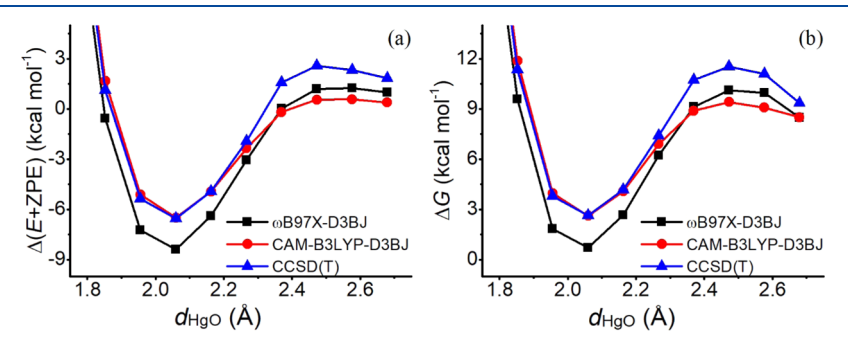
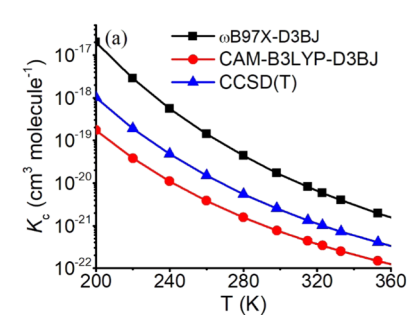


Figure 11. ZPE-corrected energy (a) and Gibbs free energy (b) profiles along the $d_{\rm HgO}$ distance at 298.15 K. Energies have been calculated with respect to the reactants separated at infinite distance. The ZPE and $G_{\rm corr}$ applied to the CCSD(T) energies along the path were taken from ω B97X-D3BJ thermochemistry. The energy corrections for the reactants were obtained directly from CCSD(T) optimizations and frequency calculations.



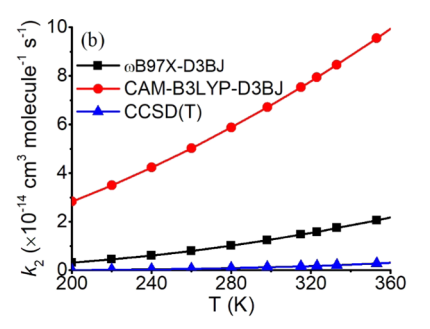


Figure 12. (a) Equilibrium constant $K_c(T)$ for the reaction BrHg + $O_2 \rightleftharpoons$ BrHgOO. (b) Rate constants $k_2(T)$ for the formation of BrHgOO.

ı

The low-pressure limiting rate constant $k_0(T)$ could be expressed as (shown in Figure S6)

$$k_0(T) = k_0(298 \text{ K}) \left(\frac{298}{T}\right)^{-1.43}$$
 (4)

where $k_0(298 \text{ K}) = 7.0 \times 10^{-38} \text{ cm}^6 \text{ molecule}^{-2} \text{ s}^{-1}$.

The major fate of BrHg in the atmosphere appears to be the reaction with ozone. While the low rate of reaction R2 makes it unlikely to be at or near equilibrium, the computed equilibrium constant provides an upper limit on the abundance of BrHgOO relative to BrHg. Figure 13 shows the equilibrium

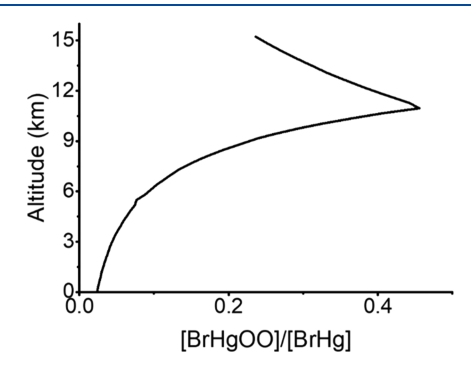


Figure 13. Equilibrium ratio of [BrHgOO] to [BrHg] as a function of altitude for U.S. Standard Atmosphere, using CCSD(T) value of $K_c(T)$.

ratio, [BrHgOO]/[BrHg], versus altitude for U.S. Standard Atmosphere.⁸⁸ The ratio is about 0.02 at ground level. Because the ratio is highest at low temperatures, it rises rapidly to a maximum of nearly 0.46 at the tropopause and then falls with increasing altitude. We also expect non-negligible equilibrium ratios of [BrHgOO] to [BrHg] during polar winters at ground level (e.g., 0.19 at 250 K). These results suggest that BrHgOO could be a significant intermediate in Br-initiated oxidation of Hg⁽⁰⁾ under some atmospheric conditions. For that reason, we carried out a preliminary investigation of reactions of BrHgOO with the atmospheric radicals NO, NO₂, and HOO. The results shown in Table 2 indicate that BrHgOO can react exothermically with these radicals in much the same way as would HOO or an organic peroxy radical.89-91 That is, it combines with NO_x and HOO, forming weak covalent bonds. In addition, it reacts exothermically with NO to form BrHgO + NO_2 and with HOO to form BrHgOOH + O_2 .

IV. CONCLUSIONS

We determined the rate constant of the reaction of BrHg and NO, k_1 , to be $7.0^{+1.3}_{-0.9} \times 10^{-12}$ cm³ molecule⁻¹ s⁻¹ in the N₂ bath

Table 2. Enthalpy of Reaction (kcal mol⁻¹ at 0 K) of Some Possible Reactions of BrHgOO in the Atmosphere at the PBEO/AVTZ Level of Theory

reaction	$\Delta H_{\rm r}^{\circ} \ (0 \ {\rm K})$
$BrHgOO + NO \rightarrow BrHgO + NO_2$	-9.1
$BrHgOO + NO \rightarrow BrHgOONO$	-18.2
$BrHgOO + NO_2 \rightarrow BrHgOONO_2$	-18.9
BrHgOO + HOO → BrHgOOOOH	-5.4
$BrHgOO + HOO \rightarrow BrHgOOH + O_2$	-29.7

over the range of pressure and temperature of 50-700 Torr and 315-353 K, respectively. Our theoretical work confirms that this reaction proceeds to Hg + BrNO without a barrier, which is consistent with the observed lack of temperature dependence. This reaction corresponds to reduction of Hg^(I) to Hg⁽⁰⁾. The products of the oxidation channel of the reaction BrHg + NO (BrHgNO) appear to be unimportant, as suggested previously. 13 Our study of BrHg + NO shows the potential for BrHg to react at both the Br and Hg atoms, leading to reduction and oxidation, respectively. The reaction R1 represents a new reduction channel of atmospheric mercury, which, along with the analogous reduction reaction for BrHg + NO₂, 16,17 should be adopted by modelers in the simulation of mercury redox chemistry. Furthermore, similar reduction reactions may be possible for ClHg, which is a key intermediate in mercury oxidation in the stratosphere. This is supported by the exploration of the minimum energy path for ClHg + NO \rightarrow Hg + BrNO at ω B97X-D3BJ/AVTZ. Chlorine and bromine are used in coal-fired power plants to drive mercury oxidation, as part of efforts to limit mercury emissions. 92 Some present models of Hg(0) oxidation in these power plants suggest that NO inhibits Hg(0) oxidation by Cl and Br, while experiments show no effect of NO. 92-94 If those models were to include reduction of Hg(I) to Hg(0) in reactions of ClHg and BrHg with NO and NO2, this discrepancy would be exacerbated.

Our experimental investigation of the reaction BrHg + O_2 revealed no evidence for this reaction, and our theoretical work confirms that the reaction is too slow to occur on the short time scales of our experiment. The LIF signal of BrHg is found to experience fluorescence quenching at a rate constant of (1.7 \pm 0.1) \times 10⁻¹⁰ cm³ molecule⁻¹ s⁻¹, close to the published result. The kinetics pathways (reactions R3–R5) illustrated in Figure 10 potentially lead to a decrease of the BrHg LIF signals in the presence of O_2 , which challenges efforts to measure the rate constant using LIF spectroscopy. Different techniques that can capture the temporal behavior of [BrHg(\tilde{X})] are needed to study the kinetics of BrHg reactions in the presence of O_2 . The computed equilibrium constant for

this reaction suggests that a non-negligible fraction of BrHg may be stored as BrHgOO in the upper troposphere and in polar winters at ground level. Our computations suggest that the reaction is at or near the low-pressure limit under atmospheric conditions. The computed forward rate constants, $k_2([M], T)$, and rate constants, K_{c} , will enable scientists to consider this chemistry in kinetic models. We present preliminary results indicating that BrHgOO reacts with atmospheric radicals in much the same manner as HOO or organic peroxy radicals. We look forward to investigations of the kinetics of such reactions.

ASSOCIATED CONTENT

Supporting Information

The Supporting Information is available free of charge at https://pubs.acs.org/doi/10.1021/acs.jpca.2c02531.

Values of pseudo-first-order rate constants of BrHg + NO in experiments; molecular orbitals of BrHgNO; ZPE-corrected Gibbs free energy profiles for BrHg + NO; T_1 diagnostic for BrHg reaction with NO and O_2 ; pressure and temperature dependence of rate constants to form BrHgOO; computed rate constants and equilibrium constants of BrHg + O_2 ; and Cartesian coordinates (PDF)

AUTHOR INFORMATION

Corresponding Authors

Theodore S. Dibble – Department of Chemistry, State University of New York College of Environmental Science and Forestry, Syracuse, New York 13210, United States; orcid.org/0000-0002-0023-8233; Phone: (315) 470-

6596; Email: tsdibble@esf.edu

Chuji Wang — Department of Physics and Astronomy, Mississippi State University, Mississippi State, Mississippi 39762, United States; Phone: (662) 325-9455; Email: cw175@msstate.edu

Authors

Rongrong Wu — Department of Physics and Astronomy, Mississippi State University, Mississippi State, Mississippi 39762, United States; Occid.org/0000-0002-8617-468X

Pedro J. Castro – Department of Chemistry, State University of New York College of Environmental Science and Forestry, Syracuse, New York 13210, United States; orcid.org/0000-0003-1650-4708

Cameron Gaito — Department of Physics and Astronomy, Mississippi State University, Mississippi State, Mississippi 39762, United States

Kyle Beiter – Department of Chemistry, State University of New York College of Environmental Science and Forestry, Syracuse, New York 13210, United States

Complete contact information is available at: https://pubs.acs.org/10.1021/acs.jpca.2c02531

Notes

The authors declare no competing financial interest.

ACKNOWLEDGMENTS

This material is based upon the work supported by the National Science Foundation under Grant Numbers 1609848, 2004100, and 2108712. The authors thank Dr. Zhiyong Gong and Josh Cohen for developing the data acquisition software.

REFERENCES

- (1) AMAP/UN Environment. Technical Background Report for the Global Mercury Assessment 2018; Arctic Monitoring and Assessment Programme, Oslo, Norway/UN Environment Programme, Chemicals and Health Branch: Geneva, Switzerland, 2019.
- (2) Lyman, S. N.; Cheng, I.; Gratz, L. E.; Weiss-Penzias, P.; Zhang, L. An Updated Review of Atmospheric Mercury. *Sci. Total Environ.* **2020**, 707, No. 135575.
- (3) Driscoll, C. T.; Mason, R. P.; Chan, H. M.; Jacob, D. J.; Pirrone, N. Mercury as a Global Pollutant: Sources, Pathways, and Effects. *Environ. Sci. Technol.* **2013**, *47*, 4967–4983.
- (4) Ariya, P. A.; Amyot, M.; Dastoor, A.; Deeds, D.; Feinberg, A.; Kos, G.; Poulain, A.; Ryjkov, A.; Semeniuk, K.; Subir, M.; Toyota, K. Mercury Physicochemical and Biogeochemical Transformation in the Atmosphere and at Atmospheric Interfaces: A Review and Future Directions. *Chem. Rev.* **2015**, *115*, 3760–3802.
- (5) Lin, C. J.; Pongprueksa, P.; Lindberg, S. E.; Pehkonen, S. O.; Byun, D.; Jang, C. Scientific Uncertainties in Atmospheric Mercury Models I: Model Science Evaluation. *Atmos. Environ.* **2006**, *40*, 2911–2928.
- (6) Goodsite, M. E.; Plane, J. M. C.; Skov, H. A. Theoretical Study of the Oxidation of Hg⁰ to HgBr₂ in the Troposphere. *Environ. Sci. Technol.* **2004**, 38, 1772–1776.
- (7) Filatov, M.; Cremer, D. Revision of the Dissociation Energies of Mercury Chalcogenides Unusual Types of Mercury Bonding. *ChemPhysChem* **2004**, *5*, 1547–1557.
- (8) Calvert, J. G.; Lindberg, S. E. Mechanisms of Mercury Removal by O₃ and OH in the Atmosphere. *Atmos. Environ.* **2005**, *39*, 3355–3367
- (9) Dibble, T. S.; Tetu, H. L.; Jiao, Y.; Thackray, C. P.; Jacob, D. J. Modeling the OH-Initiated Oxidation of Mercury in the Global Atmosphere without Violating Physical Laws. *J. Phys. Chem. A* **2020**, 124, 444–453.
- (10) Shah, V.; Jacob, D. J.; Thackray, C. P.; Wang, X.; Dibble, T. S.; Saiz-Lopez, A.; Černušák, I.; Kellö, V.; Castro, P. J.; Wu, R.; et al. Improved Mechanistic Model of the Atmospheric Redox Chemistry of Mercury. *Environ. Sci. Technol.* **2021**, *55*, 14445–14456.
- (11) Donohoue, D. L.; Bauer, D.; Cossairt, B.; Hynes, A. J. Temperature and Pressure Dependent Rate Coefficients for the Reaction of Hg with Br and the Reaction of Br with Br: A Pulsed Laser Photolysis-Pulsed Laser Induced Fluorescence Study. *J. Phys. Chem. A* **2006**, *110*, 6623–6632.
- (12) Saiz-Lopez, A.; Ulises Acuña, A.; Trabelsi, T.; Carmona-García, J.; Dávalos, J. Z.; Rivero, D.; Cuevas, C. A.; Kinnison, D. E.; Sitkiewicz, S. P.; Roca-Sanjuán, D.; Francisco, J. S. Gas-Phase Photolysis of Hg(I) Radical Species: A New Atmospheric Mercury Reduction Process. *J. Am. Chem. Soc.* **2019**, *141*, 8698–8702.
- (13) Dibble, T. S.; Zelie, M. J.; Mao, H. Thermodynamics of Reactions of ClHg and BrHg Radicals with Atmospherically Abundant Free Radicals. *Atmos. Chem. Phys.* **2012**, *12*, 10271–10279.
- (14) Dibble, T. S.; Zelie, M. J.; Mao, H. Corrigendum to 'Thermodynamics of Reactions of ClHg and BrHg Radicals with Atmospherically Abundant Free Radicals' published in Atmos. Chem. Phys. 12, 10271–10279, 2012. Atmos. Chem. Phys. 2013, 13, 9211–9212.
- (15) Dibble, T. S.; Schwid, A. C. Thermodynamics Limits the Reactivity of BrHg Radical with Volatile Organic Compounds. *Chem. Phys. Lett.* **2016**, *659*, 289–294.
- (16) Jiao, Y.; Dibble, T. S. First Kinetic Study of the Atmospherically Important Reactions BrHg• + NO₂ and BrHg• + HOO. *Phys. Chem. Phys.* **2017**, *19*, 1826–1838.
- (17) Wu, R.; Wang, C.; Dibble, T. S. First Experimental Kinetic Study of the Atmospherically Important Reaction of BrHg + NO_2 . Chem. Phys. Lett. **2020**, 759, No. 137928.
- (18) Jiao, Y.; Dibble, T. S. Quality Structures, Vibrational Frequencies, and Thermochemistry of the Products of Reaction of BrHg• with NO₂, HO₂, ClO, BrO, and IO. *J. Phys. Chem. A* **2015**, 119, 10502–10510.

- (19) Horowitz, H. M.; Jacob, D. J.; Zhang, Y.; Dibble, T. S.; Slemr, F.; Amos, H. M.; Schmidt, J. A.; Corbitt, E. S.; Marais, E. A.; Sunderland, E. M. A New Mechanism for Atmospheric Mercury Redox Chemistry: Implications for the Global Mercury Budget. *Atmos. Chem. Phys.* **2017**, *17*, 6353–6371.
- (20) Wang, S.; McNamara, S. M.; Moore, C. W.; Obrist, D.; Steffen, A.; Shepson, P. B.; Staebler, R. M.; Raso, A. R. W.; Pratt, K. A. Direct Detection of Atmospheric Atomic Bromine Leading to Mercury and Ozone depletion. *Proc. Natl. Acad. Sci. U.S.A.* **2019**, *116*, 14479–14484.
- (21) Obrist, D.; Tas, E.; Peleg, M.; Matveev, V.; Faïn, X.; Asaf, D.; Luria, M. Bromine-Induced Oxidation of Mercury in the Mid-Latitude Atmosphere. *Nat. Geosci.* **2011**, *4*, 22–26.
- (22) Wang, F.; Saiz-Lopez, A.; Mahajan, A. S.; Gómez Martín, J. C.; Armstrong, D.; Lemes, M.; Hay, T.; Prados-Roman, C. Enhanced Production of Oxidised Mercury over the Tropical Pacific Ocean: A Key Missing Oxidation Pathway. *Atmos. Chem. Phys.* **2014**, *14*, 1323–1335.
- (23) Gratz, L. E.; Ambrose, J. L.; Jaffe, D. A.; Shah, V.; Jaeglé, L.; Stutz, J.; Festa, J.; Spolaor, M.; Tsai, C.; Selin, N. E.; et al. Oxidation of Mercury by Bromine in the Subtropical Pacific Free Troposphere. *Geophys. Res. Lett.* **2015**, *42*, 10494–10502.
- (24) Saiz-Lopez, A.; Travnikov, O.; Thackray, C. P.; Jacob, D. J.; Carmona-García, J.; Francés-Monerris, A.; Roca-Sanjuán, D.; Ulises Acuña, A.; Dávalos, J. Z.; et al. Photochemistry of Oxidized Hg(I) and Hg(II) Species Suggests Missing Mercury Oxidation in the Troposphere. *Proc. Natl. Acad. Sci. U.S.A.* **2020**, *117*, 30949–30956.
- (25) Gomez Martin, J. C.; Lewis, T. R.; Douglas, K. M.; Blitz, M.; Saiz-Lopez, A.; Plane, J. M. C. The Reaction Between HgBr and O₃: kinetic study and atmospheric implications (in press). *Phys. Chem. Chem. Phys.* **2022**, 12419.
- (26) Holmes, C. D.; Jacob, D. J.; Corbitt, E. S.; Mao, J.; Yang, X.; Talbot, R.; Slemr, F. Global Atmospheric Model for Mercury Including Oxidation by Bromine Atoms. *Atmos. Chem. Phys.* **2010**, 10, 12037–12057.
- (27) Saiz-Lopez, A.; Sitkiewicz, S. P.; Roca-Sanjuán, D.; Oliva-Enrich, J. M.; Dávalos, J. Z.; Notario, R.; Jiskra, M.; Xu, Y.; Wang, F.; Thackray, C. P.; et al. Photoreduction of Gaseous Oxidized Mercury Changes Global Atmospheric Mercury Speciation, Transport and Deposition. *Nat. Commun.* **2018**, *9*, No. 4796.
- (28) Francés-Monerris, A.; Carmona-García, J.; Ulises Acuña, A.; Dávalos, J. Z.; Cuevas, C. A.; Kinnison, D. E.; Francisco, J. S.; Saiz-Lopez, A.; Roca-Sanjuán, D. Photodissociation Mechanisms of Major Mercury(II) Species in the Atmospheric Chemical Cycle of Mercury. *Angew. Chem., Int. Ed.* **2020**, *59*, 7605–7610.
- (29) Sitkiewicz, S. P.; Rivero, D.; Oliva-Enrich, J. M.; Saiz-Lopez, A.; Roca-Sanjuán, D. *Ab initio* Quantum-Chemical Computations of the Absorption Cross Sections of HgX₂ and HgXY (X, Y = Cl, Br, and I): Molecules of Interest in the Earth's Atmosphere. *Phys. Chem. Chem. Phys.* **2019**, 21, 455–467.
- (30) Lam, K. T.; Wilhelmsen, C. J.; Schwid, A. C.; Jiao, Y.; Dibble, T. S. Computational Study on the Photolysis of BrHgONO and the Reactions of BrHgO with CH₄, C₂H₆, NO, and NO₂: Implications for Formation of Hg(II) Compounds in the Atmosphere. *J. Phys. Chem. A* **2019**, *123*, 1637–1647.
- (31) Lin, C. J.; Pehkonen, S. O. The Chemistry of Atmospheric Mercury: A Review. *Atmos. Environ.* **1999**, 33, 2067–2079.
- (32) Munthe, J.; McElroy, W. J. Some Aqueous Reactions of Potential Importance in the Atmospheric Chemistry of Mercury. *Atmos. Environ.*, Part A 1992, 26, 553–557.
- (33) Gårdfeldt, K.; Jonsson, M. Is Bimolecular Reduction of Hg(II) Complexes Possible in Aqueous Systems of Environmental Importance. *J. Phys. Chem. A* **2003**, *107*, 4478–4482.
- (34) Si, L.; Ariya, P. A. Reduction of Oxidized Mercury Species by Dicarboxylic Acids (C_2 - C_4): Kinetic and Product Studies. *Environ. Sci. Technol.* **2008**, *42*, 5150–5155.
- (35) Pehkonen, S. O.; Lin, C. J. Aqueous Photochemistry of Mercury with Organic Acids. *J. Air Waste Manage. Assoc.* **1998**, 48, 144–150.

- (36) Lin, C. J.; Pehkonen, S. O. Two-Phase Model of Mercury Chemistry in the Atmosphere. *Atmos. Environ.* **1998**, 32, 2543–2558.
- (37) Amos, H. M.; Jacob, D. J.; Holmes, C. D.; Fisher, J. A.; Wang, Q.; Yantosca, R. M.; Corbitt, E. S.; Galarneau, E.; Rutter, A. P.; Gustin, M. S.; et al. Gas-Particle Partitioning of Atmospheric Hg(II) and Its Effect on Global Mercury Deposition. *Atmos. Chem. Phys.* **2012**, *12*, 591–603.
- (38) Tong, Y.; Eichhorst, T.; Olson, M. R.; Rutter, A. P.; Shafer, M. M.; Wang, X.; Schauer, J. J. Comparison of Heterogeneous Photolytic Reduction of Hg(II) in the Coal Fly Ashes and Synthetic Aerosols. *Atmos. Res.* **2014**, *138*, 324–329.
- (39) Khiri, D.; Louis, F.; Černušák, I.; Dibble, T. S. BrHgO• + CO: Analogue of OH + CO and Reduction Path for Hg(II) in the Atmosphere. ACS Earth Space Chem. 2020, 4, 1777−1784.
- (40) Tong, Y.; Zhang, H.; Lin, H.; Foy, B.; Chen, L.; Zhang, W.; Wang, X.; Guan, C. A Potential Route for Photolytic Reduction of HgCl₂ and HgBr₂ in Dry Air and Analysis about the Impacts from Ozone. *Atmos. Res.* **2021**, *249*, No. 105310.
- (41) Subir, M.; Ariya, P. A.; Dastoor, A. P. A Review of Uncertainties in Atmospheric Modeling of Mercury Chemistry I. Uncertainties in Existing Kinetic Parameters Fundamental Limitations and the Importance of Heterogeneous Chemistry. *Atmos. Environ.* **2011**, *45*, 5664–5676.
- (42) Travnikov, O.; Chételat, J.; Brian, M.; Hickey, C.; Poulain, A. J.; Dastoor, A.; Ryjkov, A.; McAlpine, D.; Vanderwolf, K.; Jung, T. S.; Hale, L.; Cooke, E. L. L.; et al. Multi-Model Study of Mercury Dispersion in the Atmosphere: Atmospheric Processes and Model Evaluation. *Atmos. Chem. Phys.* **2017**, *17*, 5271–5295.
- (43) Ye, Z.; Mao, H.; Driscoll, C. T.; Wang, Y.; Zhang, Y.; Jaeglé, L. Evaluation of CMAQ Coupled with a State-of-the-Art Mercury Chemical Mechanism (CMAQ-newHg-Br). *J. Adv. Model. Earth Syst.* **2018**, *10*, 668–690.
- (44) Zhang, L.; Lyman, S.; Mao, H.; Lin, C.-J.; Gay, D. A.; Wang, S.; Gustin, M. S.; Feng, X.; Wania, F. A. Synthesis of Research Needs for Improving the Understanding of Atmospheric Mercury Cycling. *Atmos. Chem. Phys.* **2017**, *17*, 9133–9144.
- (45) Burkholder, J. B.; Sander, S. P.; Abbatt, J.; Barker, J. R.; Cappa, C.; Crounse, J. D.; Dibble, T. S.; Huie, R. E.; Kolb, C. E.; Kurylo, M. J. et al. *Chemical Kinetics and Photochemical Data for Use in Atmospheric Studies*, Evaluation No. 19. JPL Publication 19-5; Jet Propulsion Laboratory: Pasadena, 2019.
- (46) Tong, X.; Barat, R. B.; Poulos, A. T. Detection of Mercuric Bromide in a Gas Phase Flow Cell by Laser Photofragment Fluorescence Spectroscopy. *Environ. Sci. Technol.* **1999**, 33, 3260–3263.
- (47) Lide, D. R. CRC Handbook of Chemistry and Physics, 84th ed.; CRC Press LLC: Cleveland, Ohio, 2003.
- (48) Levaggi, D. A.; Siu, W.; Feldstein, M.; Kothny, E. L. Quantitative Separation of Nitric Oxide from Nitrogen Dioxide at Atmospheric Concentration Ranges. *Environ. Sci. Technol.* **1972**, *6*, 250–252.
- (49) Ai, Y.; Li, J.; Li, Q.; Sun, M.; Li, Y.; Wang, C. Cavity Ringdown Spectroscopy of Nitric Oxide in the Ultraviolet Region for Human Breath Test. J. Breath Res. 2020, 14, No. 037101.
- (50) Donohoue, D. L. Kinetic Studies of the Oxidation Pathways of Gaseous Elemental Mercury. Ph.D. Dissertation, University of Miami, 2008.
- (51) Greig, G.; Gunning, H. E.; Strausz, O. P. Reactions of Metal Atoms. II. The Combination of Mercury and Bromine Atoms and the Dimerization of HgBr. *J. Chem. Phys.* **1970**, *52*, 3684–3690.
- (52) Maya, J. Ultraviolet Absorption Cross Sections of HgI₂, HgBr₂, and Tin (II) Halide Vapors. *J. Chem. Phys.* **1977**, *67*, 4976–4980.
- (53) Dunning, T. H., Jr. Gaussian Basis Sets for Use in Correlated Molecular Calculations. I. The Atoms Boron Through Neon and Hydrogen. *J. Chem. Phys.* **1989**, *90*, 1007.
- (54) Peterson, K. A.; Woon, D. E.; Dunning, T. H., Jr. Benchmark Calculations with Correlated Molecular Wave Functions. IV. The Classical Barrier Height of the $H + H_2 \rightarrow H_2 + H$ reaction. *J. Chem. Phys.* **1994**, *100*, 7410–7415.

- (55) Peterson, K. A.; Figgen, D.; Goll, E.; Stoll, H.; Dolg, M. Systematically Convergent Basis Sets with Relativistic Pseudopotentials. II. Small-Core Pseudopotentials and Correlation Consistent Basis Sets for the Post-*d* Group 16–18 Elements. *J. Chem. Phys.* **2003**, 119, 11113.
- (56) Figgen, D.; Rauhut, G.; Dolg, M.; Stoll, H. Energy-Consistent Pseudopotentials for Group 11 and 12 Atoms: Adjustment to Multi-Configuration Dirac—Hartree—Fock Data. *Chem. Phys.* **2005**, *311*, 227.
- (57) Peterson, K. A.; Puzzarini, C. Systematically Convergent Basis Sets for Transition Metals. II. Pseudopotential-Based Correlation Consistent Basis Sets for the Group 11 (Cu, Ag, Au) and 12 (Zn, Cd, Hg) Elements. *Theor. Chem. Acc.* 2005, 114, 283.
- (58) Purvis, G. D., III; Bartlett, R. J. A Full Coupled-Cluster Singles and Doubles Model: The Inclusion of Disconnected Triples. *J. Chem. Phys.* **1982**, *76*, 1910–1918.
- (59) Pople, J. A.; Head-Gordon, M.; Raghavachari, K. Quadratic Configuration Interaction. A General Technique for Determining Electron Correlation Energies. *J. Chem. Phys.* **1987**, *87*, 5968–5975.
- (60) Neese, F. The ORCA Program System. Wiley Interdiscip. Rev.: Comput. Mol. Sci. 2012, 2, 73–78.
- (61) Becke, A. D. Density-Functional Thermochemistry. V. Systematic Optimization of Exchange-Correlation Functionals. *J. Chem. Phys.* **1997**, 107, 8554–8560.
- (62) Grimme, S.; Ehrlich, S.; Goerigk, L. Effect of the Damping Function in Dispersion Corrected Density Functional Theory. *J. Comput. Chem.* **2011**, 32, 1456–1465.
- (63) Frisch, M. J.; Trucks, G. W.; Schlegel, H. B.; Scuseria, G. E.; Robb, M. A.; Cheeseman, J. R.; Scalmani, G.; Barone, V.; Petersson, G. A.; Nakatsuji, H. et al. *Gaussian 16*; Gaussian Inc.: Wallingford, CT, 2016.
- (64) Yanai, T.; Tew, D. P.; Handy, N. C. A New Hybrid Exchange—Correlation Functional Using the Coulomb-Attenuating Method (CAM-B3LYP). *Chem. Phys. Lett.* **2004**, 393, 51–57.
- (65) Chai, J.-D.; Head-Gordon, M. Systematic Optimization of Long-Range Corrected Hybrid Density Functionals. *J. Chem. Phys.* **2008**, *128*, No. 084106.
- (66) Grimme, S.; Antony, J.; Ehrlich, S.; Krieg, H. A Consistent and Accurate *ab initio* Parametrization of Density Functional Dispersion Correction (DFT-D) for the 94 Elements H-Pu. *J. Chem. Phys.* **2010**, 132, No. 154104.
- (67) Roos, B. O. The Complete Active Space Self-Consistent Field Method and Its Applications in Electronic Structure Calculations. *Adv. Chem. Phys.*, John Wiley & Sons, Inc., 1987; Vol. 69, p 399.
- (68) Angeli, C.; Cimiraglia, R.; Evangelisti, S.; Leininger, T.; Malrieu, J.-P. Introduction of *n*-Electron Valence States for Multi-reference Perturbation Theory. *J. Chem. Phys.* **2001**, *114*, 10252.
- (69) Angeli, C.; Cimiraglia, R.; Malrieu, J.-P. *N*-Electron Valence State Perturbation Theory: A Fast Implementation of the Strongly Contracted Variant. *Chem. Phys. Lett.* **2001**, *350*, 297–305.
- (70) Angeli, C.; Cimiraglia, R.; Malrieu, J.-P. *N*-Electron Valence State Perturbation Theory: A Spinless Formulation and an Efficient Implementation of the Strongly Contracted and of the Partially Contracted Variants. *J. Chem. Phys.* **2002**, *117*, 9138.
- (71) Schapiro, I.; Sivalingam, K.; Neese, F. Assessment of N-Electron Valence State Perturbation Theory for Vertical Excitation Energies. *J. Chem. Theory Comput.* **2013**, *9*, 3567–3580.
- (72) Angeli, C.; Borini, S.; Cestari, M.; Cimiraglia, R. A. Quasidegenerate Formulation of the Second Order N-Electron Valence State Perturbation Theory Approach. *J. Chem. Phys.* **2004**, *121*, 4043.
- (73) Barker, J. R.; Nguyen, T. L.; Stanton, J. F.; Aieta, C.; Ceotto, M.; Gabas, F.; Kumar, T. J. D.; Li, C. G. L.; Lohr, L. L.; Maranzana, A. et al. *MultiWell-2021 Software Suite*; University of Michigan: Ann Arbor, Michigan, 2021.
- (74) Barker, J. R. Multiple-Well, Multiple-Path Unimolecular Reaction Systems. I. MultiWell Computer Program Suite. *Int. J. Chem. Kinet.* **2001**, 33, 232–245.

- (75) Barker, J. R. Energy Transfer in Master Equation Simulations: A New Approach. *Int. J. Chem. Kinet.* **2009**, *41*, 748–763.
- (76) Weaver, A. B.; Alexeenko, A. A. Revised Variable Soft Sphere and Lennard-Jones Model Parameters for Eight Common Gases up to 2200 K. J. Phys. Chem. Ref. Data 2015, 44, No. 023103.
- (77) Chen, W.; Schlegel, H. B. Evaluation of S² for Correlated Wave Functions and Spin Projection of Unrestricted Mo/ller–Plesset Perturbation Theory. *J. Chem. Phys.* **1994**, *101*, 5957.
- (78) Dutta, A.; Sherrill, C. D. Full Configuration Interaction Potential Energy Curves for Breaking Bonds to Hydrogen: An Assessment of Single-Reference Correlation Methods. *J. Chem. Phys.* **2003**, *118*, 1610.
- (79) Valeur, B.; Berberan-Santos, M. N. Molecular Fluorescence: Principles and Applications, 2nd ed.; Wiley-VCH Verlag & Co. KGaA: Weinheim, Germany, 2012.
- (80) Hutchinson, M. H. R.; Theocharous, E. S. Measurement of Radiative Lifetimes and Collisional Quenching Rates of HgX(B) (X = I, Br, Cl) by VUV Photolysis of HgX_2 . Chem. Phys. Lett. 1981, 81, 553–557.
- (81) Helvajian, H.; Wittig, C. Collisional Quenching of HgBr- $(B^2\sum_{1/2}^+)$. Opt. Commun. 1979, 30, 189–192.
- (82) Waynant, R. W.; Eden, J. G. HgX(B) Radiative Lifetime by Fast Photolysis of HgX_2 (X = Br, I). Appl. Phys. Lett. 1978, 33, 708–710.
- (83) Fally, S.; Vandaele, A. C.; Carleer, M.; Hermans, C.; Jenouvrier, A.; Mérienne, M.-F.; Coquart, B.; Colin, R. Fourier Transform Spectroscopy of the O₂ Herzberg bands. III. Absorption Cross Sections of the Collision-Induced Bands and of the Herzberg Continuum. *J. Mol. Spectrosc.* **2000**, 204, 10–20.
- (84) Krupenie, P. H. The Spectrum of Molecular Oxygen. J. Phys. Chem. Ref. Data 1972, 1, 423-534.
- (85) Huber, K. P.; Herzberg, G. H. Constants of Diatomic Molecules. In *NIST Chemistry WebBook*, NIST Standard Reference Database Number 69; Linstrom, P. J.; Mallard, W. G., Eds.; National Institute of Standards and Technology: Gaithersburg, MD, 2022. http://webbook.nist.gov (retrieved May 15, 2022).
- (86) Troe, J. Predictive Possibilities of Unimolecular Rate Theory. J. Phys. Chem. A 1979, 83, 114–126.
- (87) Cobos, C. J.; Troe, J. Prediction of Reduced Falloff Curves for Recombination Reactions at Low Temperatures. *Z. Phys. Chem.* **2003**, 217, 1031–1044.
- (88) Minzner, R. A. The 1976 Standard Atmosphere and Its Relationship to Earlier Standards. Rev. Geophys. 1977, 15, 375-384.
- (89) Orlando, J. J.; Tyndall, G. S. Laboratory Studies of Organic Peroxy Radical Chemistry: An Overview with Emphasis on Recent Issues of Atmospheric Significance. *Chem. Soc. Rev.* **2012**, *41*, 6294–6317.
- (90) Hou, H.; Wang, B. Systematic Computational Study on the Reactions of HO $_2$ with RO $_2$: The HO $_2$ + CH $_3$ O $_2$ (CD $_3$ O $_2$) and HO $_2$ + CH $_2$ FO $_2$ Reactions. *J. Phys. Chem. B* **2005**, *109*, 451–460.
- (91) Atkinson, R. Gas-Phase Tropospheric Chemistry of Organic Compounds: A Review. *Atmos. Environ.* **2007**, *41*, 200–240.
- (92) Senior, C.; Granite, E.; Linak, W.; Seames, W. Chemistry of Trace Inorganic Elements in Coal Combustion Systems: A Century of Discovery. *Energy Fuels* **2020**, *34*, 15141–15168.
- (93) Auzmendi-Murua, I.; Bozzelli, J. W. Gas Phase Mercury Oxidation by Halogens (Cl, Br, I) in Combustion Effluents: Influence of Operating Conditions. *Energy Fuels* **2016**, *30*, 603–615.
- (94) Van Otten, B.; Buitrago, P. A.; Senior, C. L.; Silcox, G. D. Gas-Phase Oxidation of Mercury by Bromine and Chlorine in Flue Gas. *Energy Fuels* **2011**, *25*, 3530–3536.